

Kirigami Engineering—Nanoscale Structures Exhibiting a Range of Controllable 3D Configurations

Xu Zhang, Lior Medina, Haogang Cai, Vladimir Aksyuk, Horacio D. Espinosa,* and Daniel Lopez*

Kirigami structures provide a promising approach to transform flat films into 3D complex structures that are difficult to achieve by conventional fabrication approaches. By designing the cutting geometry, it is shown that distinct buckling-induced out-of-plane configurations can be obtained, separated by a sharp transition characterized by a critical geometric dimension of the structures. In situ electron microscopy experiments reveal the effect of the ratio between the in-plane cut size and film thickness on out-of-plane configurations. Moreover, geometrically nonlinear finite element analyses (FEA) accurately predict the out-of-plane modes measured experimentally, their transition as a function of cut geometry, and provide the stress–strain response of the kirigami structures. The combined computational–experimental approach and results reported here represent a step forward in the characterization of thin films experiencing buckling-induced out-of-plane shape transformations and provide a path to control 3D configurations of micro- and nanoscale buckling-induced kirigami structures. The out-of-plane configurations promise great utility in the creation of micro- and nanoscale systems that can harness such structural behavior, such as optical scanning micromirrors, novel actuators, and nanorobotics. This work is of particular significance as the kirigami dimensions approach the sub-micrometer scale which is challenging to achieve with conventional micro-electromechanical system technologies.

with widespread applications in areas as diverse as biosensing, optoelectronics, energy harvesting, and many others.^[7–12] It has been demonstrated that compressive buckling, guided by predefined creases/hinges, offers the capability of fabricating elaborated 3D mesostructures on pre-stretched elastomeric substrates,^[13–15] with sizes ranging from the nano to the macroscale.^[13–17] Moreover, multifunctional materials, including piezoelectric films, have been integrated with the buckling-based morphable 3D architectures to build mechanically active 3D mesostructures.^[8] Alternatively, mechanical instability in a thin film, patterned with cuts, can also generate out-of-plane deformations under in-plane tensile loading.^[3,4,18–22] This approach is attractive from a manufacturing point of view, because it can be exploited to build 3D architectures without predefined creases, enabling the use of standard fabrication processes with high throughput. Consequently, there is considerable interest in developing design strategies to enable transformations of a planar pattern formed by cuts in a thin film, into prescribed 3D shapes. However, most of

Inspired by the ancient Japanese art of paper cutting^[1,2] and recent developments in modeling, which allow inverse design of complex shapes from a single sheet of paper,^[3–6] kirigami had emerged as a powerful strategy to transform 2D layouts into 3D complex architectures across many size scales,

the kirigami-based metamaterials and actuators reported in the literature are characterized by an in-plane critical dimension orders of magnitude larger than the film thickness^[19] and thus, the out-of-plane configurations are essentially insensitive to the thickness of the structural film. In this work, using a combined

Dr. X. Zhang
Department of Electrical and Computer Engineering
Carnegie Mellon University
Pittsburgh, PA 15213, USA


Dr. L. Medina, Prof. H. D. Espinosa
Department of Mechanical Engineering
Northwestern University
Evanston, IL 60208, USA
E-mail: espinosa@northwestern.edu

Dr. L. Medina, Prof. H. D. Espinosa
Theoretical and Applied Mechanics
Northwestern University
Evanston, IL 60208, USA

Dr. H. Cai
Tech4Health Institute and Department of Radiology
NYU Langone Health
New York, NY 10016, USA

Dr. V. Aksyuk
Microsystems and Nanotechnology Division
National Institute of Standards and Technology
Gaithersburg, MD 20899, USA

Dr. D. Lopez
Department of Electrical Engineering and Materials Research Institute
Penn State University
University Park, PA 16802, USA
E-mail: dlopez@psu.edu

 The ORCID identification number(s) for the author(s) of this article can be found under <https://doi.org/10.1002/adma.202005275>.

DOI: 10.1002/adma.202005275

experimental and numerical approach, we investigate the buckling-induced out-of-plane transformations at the limit where the in-plane dimensions approach the sheet thickness. As characteristic dimensions of mechanical devices shrink to the nanoscale, most nanomechanical devices are likely to approach this limit and thus, it is of interest to consider how kirigami-based nanoscale actuators might effectively capitalize on buckling-induced transformations.

We show nanostructures exhibiting competing symmetric and anti-symmetric 3D configurations, produced from a single planar pattern, which can be precisely controlled by: a) the ratio of the in-plane dimensions to the film thickness, and b) the intrinsic tensile stress of the structural thin films. Moreover, within the parameter space we identify an approximately linear relation between the in-plane dimensions corresponding to a sharp transition boundary between the symmetric and anti-symmetric buckling-induced out-of-plane configurations. Our work provides a relation between the in-plane geometrical parameters, the sheet thickness, and the deployed 3D shape. The reported results would be useful for the development of kirigami-based micro- and nanoactuators, with specific applications to NEMS-based switches,^[23] spatial light modulators,^[24] nanoscale grippers,^[25] and optical metasurfaces.^[26]

One of the simplest sets of cuts used to generate kirigami structures is shown in **Figure 1A–C**. It consists only of perpendicular cuts resulting in two suspended identical panels (with in-plane size $L_a \times L_b$ and thickness d) connected through hinged regions in the middle. The cut along the line separating the two panels has width c , while the hinge length is labelled as h (Figure 1B). Similar patterns have been studied in detail due to its simplicity and potential to build 3D architectures.^[3,18,19,22,27–29] Experimentally, we used focused ion beam (FIB) as a direct-write “nanocutter” to fabricate these 2D flat patterns on suspended silicon nitride (SiN_x) membranes (see Figure 1 and Experimental Section). A SEM image of a nominally 200 nm thick kirigami structure is shown in Figure 1C, which remains flat after fabrication. Since the fabricated membranes are subjected to a tensile stress, $\sigma_{xx} = N_{xx}/d$ (where N_{xx} is the membrane load per unit length), the intrinsic stress in the membrane can be used to spontaneously deploy 3D configurations. The cut free edge perpendicular to the y direction remained stress free. SiN_x membranes with as-deposited tensile stress between 400 and 500 MPa were investigated.

Interestingly, fabricating these arrays of cuts in a nominally 100 nm thick SiN_x membrane causes the suspended panels to show out-of-plane tilting behaviors. By varying the

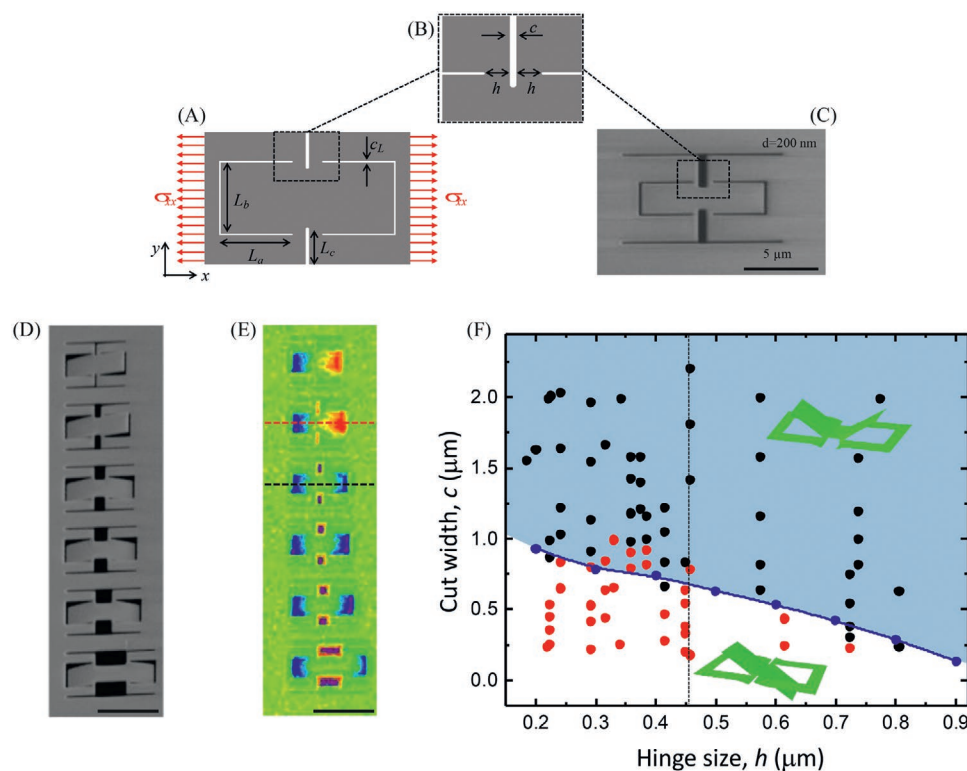


Figure 1. A) A schematic illustration of a kirigami unit cell with thickness d . B) The hinges and cuts in the middle part are the critical components that determine the kirigami tilting configuration. The geometric parameters are reported in Table 1. C) SEM image of a kirigami structure with a nominal thickness of 200 nm (tilted view: 52°). D) SEM images of an array of kirigami structures with the same hinge size, $h \approx 457$ nm and varying cut values (tilted view: 52°). The membrane nominal thickness is 100 nm. Scale bar: 10 μm . From top to bottom: $c \approx 243$ nm; $c \approx 600$ nm; $c \approx 1.45$ μm ; $c \approx 1.87$ μm ; $c \approx 2.25$ μm ; $c \approx 4.35$ μm . E) Optical profilometer images of the kirigami array shown in (D). F) Experimental diagram showing the kirigami tilting modes as a function of h (hinge size) and c (cut width). Black circles: Symmetric tilting modes; Red circles: Antisymmetric tilting modes. The reported size uncertainties are comparable to the size of the dots and given by the width of the SEM point spread function obtained by imaging a structure edge. Blue circles: FE simulation results indicating the transition between symmetric and antisymmetric modes as a function of in-plane dimensions.

Table 1. Geometric and material parameters used in the FE model.

Dimension	Description
$d = 0.1 \mu\text{m}$	Thickness
$L_b = 3.5 \mu\text{m}$	Inner plate width
$L_a = 3.5 \mu\text{m}$	Horizontal cut length
$c_L = 0.1 \mu\text{m}$	Horizontal cut width
$L_c = 1.75 \mu\text{m}$	Vertical hinge-cut length
$c = 0.1 \mu\text{m}$	Vertical hinge-cut width
$e = 1 \mu\text{m}$	Vertical cut distance to the clamped edge
$e_{\perp} = 1.5 \mu\text{m}$	Horizontal cut distance to the free edge
$E = 250 \text{ GPa}$	SiN_x Young's modulus
$\nu = 0.23$	SiN_x Poisson's ratio
$\rho = 3100 \text{ kg m}^{-3}$	SiN_x density

cutting geometry of the planar pattern, i.e., the width c and hinge length h , two distinctive out-of-plane modes, symmetric and antisymmetric, can be designed. The results depicted in Figure 1D, are SEM images of deployed kirigami structures with varying cut width c , while the hinge size, h , and all other geometric parameters are kept constant (Table 1). Figure 1E shows the optical profile of the same structures. The top kirigami structures displayed in Figure 1D–E correspond to the smallest c value, and exhibit an antisymmetric tilting configuration, i.e., the left panel tilts downward while the right panel tilts upward. Increasing the value of c , results in structures with similar antisymmetric response, until a critical value of c is reached, beyond which symmetric tilting modes are dominant, i.e., both left and right panels tilt downward (or upward).

The existence of two distinctive tilting modes was repeatedly found in hundreds of deployed kirigami structures with different combination of c and h values, which were used to plot the configurational diagram shown in Figure 1F. The antisymmetric mode (red dots) occurs in the sub-micrometer parameter space and is separated from the symmetric mode (black dots) by a well-defined transition. For a given hinge size h , the tilting mode switches from antisymmetric to symmetric at a well-defined critical value of $c = c^*$, indicating that the energetically favorable deformation mode transitions from tilting to bending (antisymmetric to symmetric).

To gain insight into the overall behavior of the kirigami structure and the transition between antisymmetric and symmetric modes, a series of geometrically nonlinear finite element (FE) simulations, using a commercial solver, were conducted for a range of hinge and cut widths as shown in Figure 2. Since the kirigami plate is defined by its thickness d , which is small in comparison to the structure overall length and width, the structure was modeled as a shell by employing 3D S4R shell elements.^[30] A homogeneous, isotropic, linearly elastic material, with Young's modulus E and Poisson's ratio ν was used in the simulations. Several parameters were employed to assess the accuracy of the FE model. In particular, we used the rotation angle θ corresponding to a prescribed displacement of 200 nm along the x -direction (see the Supporting Information, "Convergence study for the FE analysis" section for further details). Since the problem at hand is essentially one of stability, caused

by the existence of a critical buckling load and corresponding bifurcation point, an imperfection was included in the analysis. Buckling eigenmodes were obtained for each hinge-cut-ratio configuration. Subsequently, the eigenmode corresponding to an antisymmetrical tilt was used as a small perturbation from the flat geometry.

The FE analysis aimed to find, for each h , the corresponding critical cut size c^* , for which the structure changes its behavior from an antisymmetric mode to a symmetric one. The computed symmetry transition condition is depicted in Figure 1F as a solid blue line, indicating that with increasing hinge size h , a smaller cut width c is needed to enable the transition from the antisymmetric to the symmetric mode and vice versa. As shown in the figure, the agreement with the experimental data is remarkable. By running the simulations for different materials, we found the condition to be universal, provided that the material resides in its elastic regime. More interestingly, the transition to a symmetric mode occurred even when the imperfection used in the simulation was antisymmetric.

The effect of the uniaxial tensile stress on the configuration of two different kirigami modes is shown in Figure 2. As the stress σ_{xx} builds up, antisymmetric and symmetric out-of-plane configurations are predicted for a constant hinge size to thickness ratio, $h/d = 5$, and cut widths to thickness ratios of $c/d = 5$ and 6, respectively (Figure 2A,B). For both cases, the stress starts to build up around the cut corners as the uniaxial stress increases. The evolution of stresses can be visualized in the videos provided in the Supporting Information. The variation of the panel angle with the x -axis, θ , as a function of applied stress, σ_{xx} , is plotted in Figure 2C for constant values of $d = 100 \text{ nm}$, $h = 457 \text{ nm}$, and various cut widths ranging from 240 nm to $2.3 \mu\text{m}$. Before the uniaxial stress reaches a threshold value σ^* , no out-of-plane tilting can be observed. As the stress continues to build up, the onset of out-of-plane deformation occurs in both structures, as indicated by the sudden appearance of a plateau stress in the stress-angle curves (Figure 2C). The finite element analyses (FEA) figure illustrates that in all cases a buckling instability is induced in the region of the hinges with the buckling stress increasing as the cut width decreases. Notably, a discontinuous transition between the two distinctive tilting modes, which purely depends on the geometric design, is observed. When c is larger than the critical value c^* , the stress distributions are essentially symmetric with respect to the middle line, as can be seen in the right column of Figure 2A,B. We infer that such a symmetric stress distribution guides the tilt to a symmetric mode, i.e., left and right panels tilt toward the same direction. However, as the cut size c is reduced right below c^* , a sharp transition from symmetric to antisymmetric mode occurs, and the stress distribution in the structure becomes largely antisymmetric (left column of Figure 2A,B). When c is right below c^* , the left and right panels are in a strongly coupled regime, in which the tilting direction of one side dictates the other side to tilt in an opposite direction in order to minimize the overall elastic energy of the kirigami structure.^[3,19] The transition between the two (symmetric versus antisymmetric) configurations is determined by the competition between hinge bending and twisting, which also determines the coupling strength between the panels. In the limit of very large hinge

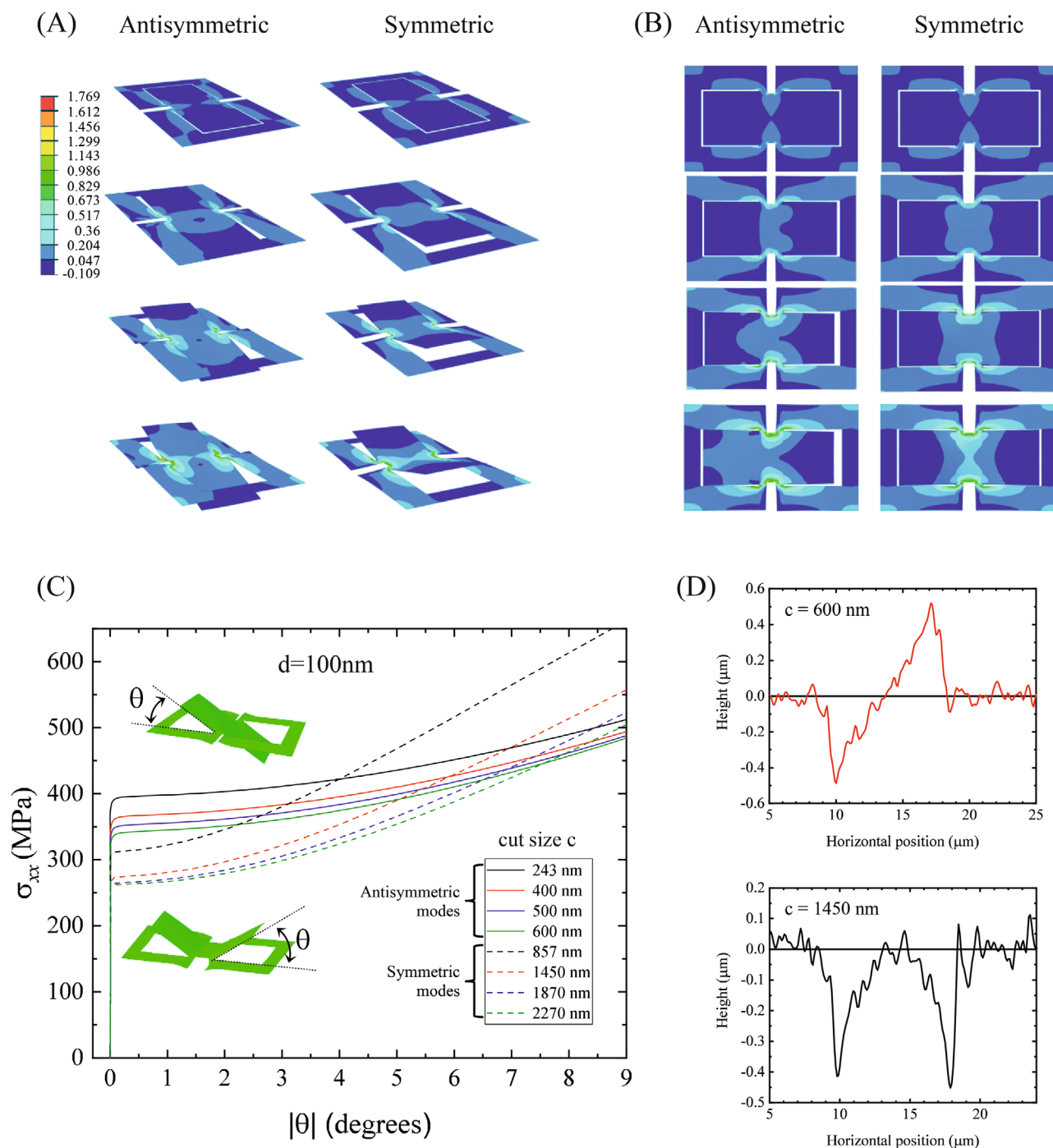


Figure 2. A) Tilted and B) top view of the FEA of the kirigami structures with plots of maximum principle in-plane stress distributions in GPa. The two kirigami structures have a hinge to thickness ratio of $h/d = 5$ and cut to thickness ratio of c/d corresponding to the antisymmetric and symmetric cases. C) Calculated stress-angle response for different values of cut c (shown in the legend), and constant $h = 457$ nm and $d = 100$ nm. Note that the angles are given in absolute values due to the stochastic behavior of the instability-induced phenomenon. D) Measured profile of the antisymmetric (top) and symmetric (bottom) kirigami modes along the dotted lines in Figure 1E.

sizes, the panels are separated far away and therefore the coupling between them is weak even when the cut size is small. That is why, as shown in Figure 1F, for larger values of h , it becomes more and more difficult to generate antisymmetric modes due to weak coupling. On the other hand, in the limit

of very small hinge sizes ($h \rightarrow 0$), the torsional stiffness of the hinges is significantly reduced and thus, they can rotate under a small stress. Notably, even when the cut size c is relatively large, it is still possible to trigger the antisymmetric tilting mode. That is why kirigami structures with smaller hinge

sizes can tolerate larger cut widths, c , before transition to the antisymmetric tilting mode.

Geometrically nonlinear FE results also reveal the stress-rotation angle responses of the kirigami structures with different values of c (Figure 2C). The solid and dashed lines represent samples displaying antisymmetric and symmetric responses, respectively, from which several observations can be made. The first is the ubiquitous presence of a bifurcation point,^[31,32] i.e., a point beyond which out-of-plane tilting is triggered, in agreement with previous reports.^[3,18,19] The threshold stress σ^* decreases as the cut width c increases for any specific hinge size h .

The out-of-plane angular displacement of the fabricated kirigami structures is shown in Figure 2D. The data were obtained using an optical profilometer and correspond to measurements along the dotted lines indicated in Figure 1E. The measured tilting angles are in good agreement with the angular displacement expected for a film having a tensile stress of about 450 MPa, corresponding to the nominal fabrication tensile stress of the used structural films. Note that in Figure 2C, the angles are given in absolute values due to the stochastic nature of instabilities, i.e., the structure can adopt 3D configurations with a negative or positive angle. In agreement with the experiments, a transition from an antisymmetric to a symmetric mode occurs for c larger than c^* . As seen in Figure 2C, a quantitative change in the stress-angle response is observed when c exceeds $c^* \approx 700$ nm. By repeating this analysis for samples with different hinge to width ratios, the locus of points where the transition occurs, was precisely determined and correspond to the blue line shown in Figure 1F.

The structural membrane thickness plays a critical role in determining the mechanical deformation of the kirigami structures. In addition to samples with a nominal thickness of 100 nm, we fabricated kirigami structures with the same geometric parameters on 200 and 50 nm thick SiN_x membranes. As shown in Figure 3A, the 200 nm thick kirigami structures remain flat after FIB milling. This indicates that the threshold stress needed to trigger the tilting mode increases as the

membrane thickness increases. Moreover, we infer that the residual stress in the 200 nm thick SiN_x membrane is below the required threshold, σ^* . When the membrane thickness was reduced to 50 nm, the kirigami structures also exhibited a sharp antisymmetric-to-symmetric tilting mode transition, Figure 3B. Stress-strain curves obtained via FEA are presented in Figure 3C. The simulations show that the threshold stress in 50 nm thick kirigami structures is much smaller than that for the 100 nm thick kirigami (inset in Figure 3C) and their tilting angles are much larger than the ones measured in the 100 nm thick structures. Interestingly, the symmetric modes observed in 50 nm structures show upward tilting, which is distinctive from the downward tilting of the 100 nm kirigami cases. We speculate that the tilting direction of the structures is determined by perturbations caused during the fabrication process and the distribution of residual stresses in the membrane, which is discussed and addressed in depth in the literature.^[33,34] In the 100 nm thick SiN_x membrane, a small stress gradient, arising from the fabrication process, might exist prior to kirigami fabrication. Such a stress gradient might guide the downward tilting direction. During the FIB milling, the Ga⁺ ion dosage could create certain vacancies in the top surface of the SiN_x membrane along the cutting edges, which only results in negligible stress gradient change in the 100 nm thick membrane. However, in a thinner 50 nm membrane, these top surface vacancies might overturn the stress gradient in the membrane and create a large enough upward tilting moment inducing the experimentally observed tilting direction, as shown in Figure 3B. Such an explanation is also consistent with the FIB-fabricated metallic kirigami structures.^[20]

In this manuscript we report the effect of the film thickness on a simple kirigami structure, which can be designed to change out-of-plane configurations when loaded by uniaxial tension. Notably, simple changes in the cut dimensions, while preserving the overall cut geometry, leads to structures exhibiting either symmetric or antisymmetric out-of-plane configurations, with mechanical deformation strongly sensitive to the thickness

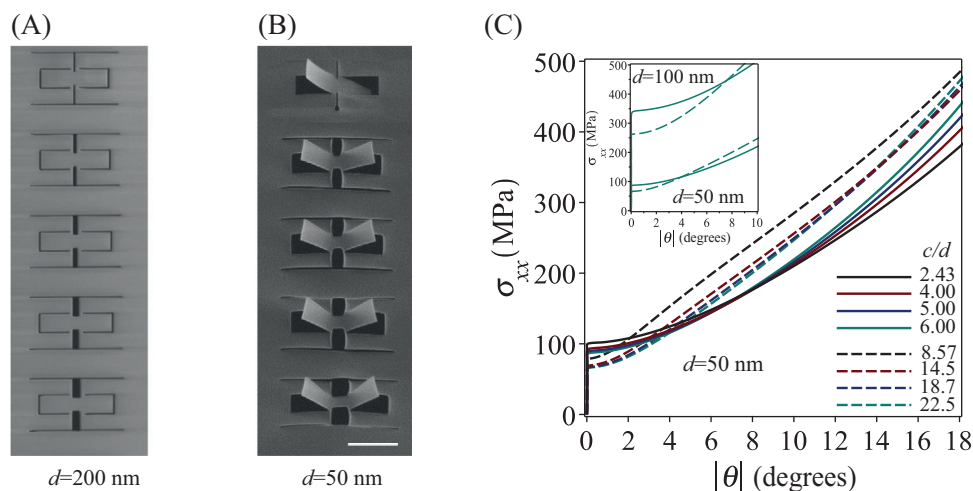


Figure 3. A,B) SEM images at 52° tilted view of kirigami structures fabricated on a 200 nm thick SiN_x membrane (A) and on a 50 nm thick SiN_x membrane (B). The kirigami dimensions in (A) and (B) are the same as those for the 100 nm thick SiN_x structures shown in Figure 1. C) FEA analysis revealing the relationship between tilting angle and uniaxial tensile stress for different c/d ratios. The inset compares the effect of the thickness d on the onset of out-of-plane deformation and angular displacement of the kirigami structures.

of the structural film. By measuring the two distinctive out-of-plane modes, symmetric and antisymmetric, we experimentally confirmed the existence of a sharp transition in the cut width-hinge size design space. Although these modes are controlled just by the geometrical parameters of the structure, the antisymmetric mode can be observed only when the hinge size is below certain threshold values, from which it was possible to extract and formulate a threshold condition for the symmetry transition between these competing buckled modes. Of particular interest is the fact that the condition is approximately linear in nature, facilitating extrapolation to all possible length scales. While the analytical derivation of the symmetry transition condition is of interest, it is beyond the scope of this work. The simulations hint at the need for a formulation, including shell buckling under shear in the hinge region, although the exact structural approximation may depend on both c/d and h/d . Hence, we leave such analytical treatment for future work. Another aspect that requires further investigation is the deterministic tilting of the structures. Potential approaches to obtain deterministic tilting includes evaporation of thin film on one side of the membrane and antisymmetric cuts to favor one specific tilting direction.

The kirigami-inspired designs reported in this work demonstrate the importance of the ratio between in-plane dimensions to sheet thickness for buckling-induced out-of-plane 3D architectures. Moreover, the elucidated symmetry breaking condition could be used to select the desired final 3D configuration of kirigami structures from two competing alternatives. Furthermore, our results reveal a range of achievable angular deformations as a function of applied uniaxial strain, which could be easily achieved by integrating kirigami structures with micro-electromechanical system (MEMS) actuators.^[35,36] In-plane stretching from a single source at its edge present a major simplification over current methods that relay on complicated, individually controlled, actuators.^[37–39] Other applications may rely on the symmetric configuration, e.g., grabbing small and delicate objects. By using such a construct, additional advantages over current methods, employed to create microtweezers, are envisioned.^[40,41] It is known that MEMS tweezers rely on a snap-through mechanism, which can be rather harsh in the case of biological samples.^[42] By contrast, in kirigami-based tweezers, the grabbing force can be precisely controlled by means of the applied uniaxial strain.

Beyond the discussed potential applications, we anticipate future endeavors in integrating such tunable structures in MEMS^[17,38] and piezoelectric transducers,^[8] for building novel 3D system and mechanisms for kirigami engineering. Particularly interesting are structures near the symmetry breaking threshold, for which the transition between competing states may be dynamically induced by an external stimulus. The possibility of controlling the transition between configuration modes would be useful for a diversity of promising applications, ranging from smart thermally actuating textiles,^[43] tunable metamaterials,^[44,45] deformable electronics,^[46] and soft-robotics.^[47–50]

Experimental Section

Finite-Element Analysis: To find the symmetry breaking condition, a series of simulations were performed for constant hinge sizes, while

the cut size was modified according to a discrete and linear search. Specifically, the discrete search began until a resolution of $\Delta c = 100$ nm was achieved and then continued with increments of $\Delta c = 10$ nm until the threshold between the two modes was obtained. Note, that all simulated structures were loaded using displacement control, with an in-plane displacement increment of $\Delta x = 200$ nm, as employed in the convergence study reported in the Supporting Information. To identify a suitable imperfection, a buckling analysis was performed for each geometry. An antisymmetric buckling mode was then used as an imperfection during the simulation under tensile loading. To select the element size, especially in the hinge region, another convergence study was carried out as reported in the Supporting Information (Figure S2, Supporting Information). Table 1 summarizes the parameters employed in the simulations.

To create the stress-rotation curves, two parameters were extracted from each simulation, the rotation at the edge of one of the flaps, and the sum of reaction forces located at the nodes of the clamped edge. For the former, the produced angles were converted from radians to degrees. To calculate the stress σ_{xx} , the summed forces were normalized against the plate clamped edge overall length and thickness.

Fabrication Methods for Silicon Nitride Kirigami Structures: The kirigami structures were fabricated with a FIB system on a suspended silicon nitride (SiN_x) membrane grown on an Si wafer with etched windows. SiN_x membranes with three different nominal thickness: 50, 100, and 200 nm were used. The nominal window size was $100 \mu\text{m} \times 100 \mu\text{m}$. The suspended SiN_x membrane had a residual tensile stress, which resulted in flat membranes to start with. The 2D kirigami patterns were directly cut by focused Ga^+ ion beam with an acceleration voltage setting of 30 kV and a current of 28 pA. The optimized ion dose used to cut the kirigami patterns was about $2.2 \text{ nC } \mu\text{m}^{-2}$. For the array of kirigami structures shown in Figure 1D, the fabrication process took about 3 min. After ion beam milling, the stretching stress in the SiN_x membrane activates the out-of-plane tilting modes and transforms the 2D kirigami patterns into 3D kirigami structures. At a current level setting of 28 pA, the overall resolution obtained with the FIB system was about 20 nm. Due to the FIB resolution limit, there will always be a small variation (up to 20 nm) of h and c values from cut to cut. After the kirigami process, the in situ SEM of the FIB system was used to measure the size of cuts and hinges.

Supporting Information

Supporting Information is available from the Wiley Online Library or from the author.

Acknowledgements

This work was performed, in part, at the Center for Nanoscale Materials, a U.S. Department of Energy Office of Science User Facility, and supported by the U.S. Department of Energy, Office of Science, under Contract No. DE-AC02-06CH11357. H.D.E. acknowledges the financial support from a Multi-University Research Initiative through the Air Force Office of Scientific Research (AFOSR-FA9550-15-1-0009), NSF through award no. DMR-1408901, and Army Research Office (ARO) through awards W911NF1510068. X.Z. acknowledges the support of Argonne National Laboratory's Laboratory Directed Research and Development (LDRD) program and the support of Carnegie Mellon University. L.M. acknowledges the support of the Tel-Aviv University – Northwestern University joint postdoctoral fellowship.

Conflict of Interest

The authors declare no conflict of interest.

Author Contributions

X.Z., D.L., and H.D.E. designed research. X.Z. and H.C. performed experimental work. L.M. and H.D.E. performed simulation work. D.L., H.D.E., X.Z., L.M., and V.A. analyzed data. D.L., H.D.E., V.A., X.Z., and L.M. wrote the paper.

Keywords

kirigami, membranes, nanofabrication, nanomechanics, nonlinearity, symmetry breaking

Received: August 3, 2020

Revised: November 3, 2020

Published online:

- [1] J. Palmer, *The Art of Papercutting*, Search Press, Tunbridge Wells, UK **2015**.
- [2] R. J. Lang, *Origami Design Secrets: Mathematical Methods for an Ancient Art*, 2nd ed., CRC Press, Boca Raton, FL, USA **2011**.
- [3] M. A. Dias, M. P. McCarron, D. Rayneau-Kirkhope, P. Z. Hanakata, D. K. Campbell, H. S. Park, D. P. Holmes, *Soft Matter* **2017**, *13*, 9087.
- [4] G. P. T. Choi, L. H. Dudte, L. Mahadevan, *Nat. Mater.* **2019**, *18*, 999.
- [5] Z. Fan, Y. Yang, F. Zhang, Z. Xu, H. Zhao, T. Wang, H. Song, Y. Huang, J. A. Rogers, Y. Zhang, *Adv. Mater.* **2020**, *32*, 1908424.
- [6] Y. Tang, G. Lin, S. Yang, Y. K. Yi, R. D. Kamien, J. Yin, *Adv. Mater.* **2017**, *29*, 1604262.
- [7] X. Guo, X. Wang, D. Ou, J. Ye, W. Pang, Y. Huang, J. A. Rogers, Y. Zhang, *npj Flexible Electron.* **2018**, *2*, 14.
- [8] M. Han, H. Wang, Y. Yang, C. Liang, W. Bai, Z. Yan, H. Li, Y. Xue, X. Wang, B. Akar, H. Zhao, H. Luan, J. Lim, I. Kandela, G. A. Ameer, Y. Zhang, Y. Huang, J. A. Rogers, *Nat. Electron.* **2019**, *2*, 26.
- [9] Z. Yan, F. Zhang, F. Liu, M. Han, D. Ou, Y. Liu, Q. Lin, X. Guo, H. Fu, Z. Xie, M. Gao, Y. Huang, J. Kim, Y. Qiu, K. Nan, J. Kim, P. Gutruf, H. Luo, A. Zhao, K.-C. Hwang, Y. Huang, Y. Zhang, J. A. Rogers, *Sci. Adv.* **2016**, *2*, 1601014.
- [10] Z. Yan, M. Han, Y. Shi, A. Badea, Y. Yang, A. Kulkarni, E. Hanson, M. E. Kandel, X. Wen, F. Zhang, Y. Luo, Q. Lin, H. Zhang, X. Guo, Y. Huang, K. Nan, S. Jia, A. W. Oraham, M. B. Mevis, J. Lim, X. Guo, M. Gao, W. Ryu, K. J. Yu, B. G. Nicolau, A. Petronico, S. S. Rubakhin, J. Lou, P. M. Ajayan, K. Thornton, G. Popescu, D. Fang, J. V. Sweedler, P. V. Braun, H. Zhang, R. G. Nuzzo, Y. Huang, Y. Zhang, J. A. Rogers, *Proc. Natl. Acad. Sci. USA* **2017**, *114*, E9455.
- [11] S. Lim, H. Luan, S. Zhao, Y. Lee, Y. Zhang, Y. Huang, J. A. Rogers, J.-H. Ahn, *Adv. Mater.* **2020**, *32*, 2001303.
- [12] A. M. Abdullah, X. Li, P. V. Braun, J. A. Rogers, K. J. Hsia, *Adv. Funct. Mater.* **2020**, *30*, 1909888.
- [13] X. Ning, X. Wang, Y. Zhang, X. Yu, D. Choi, N. Zheng, D. S. Kim, Y. Huang, Y. Zhang, J. A. Rogers, *Adv. Mater. Interfaces* **2018**, *5*, 1800284.
- [14] Y. Zhang, Z. Yan, K. Nan, D. Xiao, Y. Liu, H. Luan, H. Fu, X. Wang, Q. Yang, J. Wang, W. Ren, H. Si, F. Liu, L. Yang, H. Li, J. Wang, X. Guo, H. Luo, L. Wang, Y. Huang, J. A. Rogers, *Proc. Natl. Acad. Sci. USA* **2015**, *112*, 11757.
- [15] M. Humood, Y. Shi, M. Han, J. Lefebvre, Z. Yan, M. Pharr, Y. Zhang, Y. Huang, J. A. Rogers, A. A. Polycarpou, *Small* **2018**, *14*, 1703852.
- [16] M. Humood, Y. Shi, M. Han, J. Lefebvre, Z. Yan, M. Pharr, Y. Zhang, Y. Huang, J. A. Rogers, A. A. Polycarpou, *Small* **2018**, *14*, 1870045.
- [17] J. Rogers, Y. Huang, O. G. Schmidt, D. Gracias, *MRS Bull.* **2016**, *41*, 123.
- [18] A. Rafsanjani, K. Bertoldi, *Phys. Rev. Lett.* **2017**, *118*, 084301.
- [19] Y. Yang, M. A. Dias, D. P. Holmes, *Phys. Rev. Mater.* **2018**, *2*, 110601.
- [20] Z. Liu, H. Du, J. Li, L. Lu, Z.-Y. Li, N. X. Fang, *Sci. Adv.* **2018**, *4*, eaat4436.
- [21] M. Moshe, E. Esposito, S. Shankar, B. Bircan, I. Cohen, D. R. Nelson, M. J. Bowick, *Phys. Rev. E* **2019**, *99*, 013002.
- [22] M. Moshe, E. Esposito, S. Shankar, B. Bircan, I. Cohen, D. R. Nelson, M. J. Bowick, *Phys. Rev. Lett.* **2019**, *122*, 048001.
- [23] O. Y. Loh, H. D. Espinosa, *Nat. Nanotechnol.* **2012**, *7*, 283.
- [24] N. Savage, *Nat. Photonics* **2009**, *3*, 170.
- [25] P. Bøggild, in *Encyclopedia of Nanotechnology* (Ed: B. Bhushan), Springer, Netherlands, Dordrecht, The Netherlands **2016**, pp. 1–23.
- [26] Z. Liu, H. Du, Z.-Y. Li, N. X. Fang, J. Li, *APL Photonics* **2018**, *3*, 100803.
- [27] A. Lamoureux, K. Lee, M. Shlian, S. R. Forrest, M. Shtein, *Nat. Commun.* **2015**, *6*, 8092.
- [28] M. K. Blees, A. W. Barnard, P. A. Rose, S. P. Roberts, K. L. McGill, P. Y. Huang, A. R. Ruyack, J. W. Kevek, B. Kobrin, D. A. Muller, P. L. McEuen, *Nature* **2015**, *524*, 204.
- [29] M. Isobe, K. Okumura, *Sci. Rep.* **2016**, *6*, 24758.
- [30] Dassault Systèmes, **2019**.
- [31] G. Simitises, D. H. Hodges, *Fundamentals of Structural Stability*, 1st ed., Elsevier, **2006**.
- [32] Z. P. Bazant, L. Cedolin, *Stability of Structures: Elastic, Inelastic, Fracture and Damage Theories*, World Scientific Publishing Co., Singapore **2010**.
- [33] L. Medina, R. Gilat, B. Ilic, S. Krylov, *Sens. Actuators, A* **2014**, *220*, 323.
- [34] S. Saghier, M. L. Bellaredj, A. Ramini, M. I. Younis, *J. Micromech. Microeng.* **2016**, *26*, 095004.
- [35] S. D. Senturia, *Microsystem Design*, Springer US, New York **2001**.
- [36] H. D. Espinosa, Y. Zhu, N. Moldovan, *JMEMS* **2007**, *16*, 1219.
- [37] M. Laslandes, K. D. Patterson, S. Pellegrino, *Appl. Opt.* **2018**, *54*, 4937.
- [38] V. Aksyuk, M. Simon, F. Pardo, S. Arney, D. Lopez, A. Villanueva, "Optical MEMS design for telecommunications applications", in *Solid-State Sensor and Actuator Microsystem Workshop, Hilton Head Island, South Carolina, June 2–6, 2002*, Hilton Head Island, South Carolina **2002**, 0-9640024-4-2.
- [39] A. Uno, Y. Hirai, O. Tabata, T. Tsuchiya, in *2018 IEEE Micro Electro Mechanical Systems (MEMS)*, IEEE, Piscataway, NJ, USA **2018**, pp. 704–707.
- [40] C. Hong, S. Yang, J. C. Ndukaife, *Nat. Nanotechnol.* **2020**, *15*, 962.
- [41] H. Suzuki, R. J. Wood, *Nat. Mach. Intell.* **2020**, *2*, 437.
- [42] A. M. Alneamy, M. E. Khater, A. K. Abdel-Aziz, G. R. Heppler, E. M. Abdel-Rahman, *Int. J. Non-Linear Mech.* **2020**, *118*, 103298.
- [43] V. Sanchez, C. J. Payne, D. J. Preston, J. T. Alvarez, J. C. Weaver, A. T. Atalay, M. Boyvat, D. M. Vogt, R. J. Wood, G. M. Whitesides, C. J. Walsh, *Adv. Mater. Technol.* **2020**, *5*, 2000383.
- [44] T. Roy, S. Zhang, I. W. Jung, M. Troccoli, F. Capasso, D. Lopez, *APL Photonics* **2018**, *3*, 021302.
- [45] E. Arbabi, A. Arbabi, S. M. Kamali, Y. Horie, M. Faraji-Dana, A. Faraon, *Nat. Commun.* **2018**, *9*, 812.
- [46] S. Gupta, W. T. Navaraj, L. Lorenzelli, R. Dahiya, *npj Flexible Electron.* **2018**, *2*, 8.
- [47] C. Laschi, B. Mazzolai, M. Cianchetti, *Sci. Rob.* **2016**, *1*, eaah3690.
- [48] M. Z. Miskin, A. J. Cortese, K. Dorsey, E. P. Esposito, M. F. Reynolds, Q. Liu, M. Cao, D. A. Muller, P. L. McEuen, I. Cohen, *Nature* **2020**, *584*, 557.
- [49] A. M. Brooks, M. S. Strano, *Nature* **2020**, *584*, 530.
- [50] T. Chen, O. R. Bilal, K. Shea, C. Daraio, *Proc. Natl. Acad. Sci. USA* **2018**, *115*, 5698.